EDGE ARTICLE

Check for updates

Crown ether–cycloparaphenylene hybrid multimacrocycles: insights into supramolecular gas sensing and biological potential†

Yaning Hu,[a] Tong Li,[bc] Taotao Su,[a] Wudi Shi,[a] Yabing Yu,[a] Beibei Li,[a] Meng-Hua Li,[ID][a] Sheng Zhang,[ID][a] Yuan-Qing Xu,[a] Qi Liu,[ID]*[a] Di Wu[ID]*[b] and Youzhi Xu[ID]*[a]

The topologically intriguing multimacrocyclic architecture is endowed with distinct physical and chemical properties. The synthesis of hybrid macrocycles combining crown ethers and cycloparaphenylenes (CPPs) presents a promising strategy for developing multifunctional supramolecular systems. Herein, we first report the precise construction of a series of crown ether–CPP hybrid multimacrocycles with enhanced photophysical properties and diverse host–guest interactions. Notably, the trimacrocyclic hybrid adopts a molecular tweezer-like conformation, resulting in a significantly higher fullerene binding affinity compared to the bismacrocycle. The fullerene complex showed improved conductivity and sensitivity with a limit of detection (LOD) of 19 ppb for NO_2 with excellent cyclic stability and reliability. Additionally, the bismacrocycle exhibits significant cytotoxicity against cancer cell lines at low concentrations and enables fluorescence-based detection of inflammatory responses, highlighting its potential for biosensing applications. These findings underscore the versatility of crown ether–CPP hybrid macrocycles in supramolecular sensing and biochemistry, offering new avenues for the design of functional nanomaterials.

Introduction

In the realm of supramolecular chemistry, the synthesis and exploration of innovative macrocycles play a pivotal role in advancing materials suitable for applications in drug delivery, catalysis, sensing, and various other fields.[1] Cyclo-paraphenylenes (CPPs) represent a unique class of π-conjugated macrocycles, distinguished by their strained structure and size-dependent chemical[2] and photophysical properties.[3] These intriguing molecules have attracted considerable attention from researchers in the fields of chemistry and materials science.[4] Recent studies have highlighted the fascinating properties of topologically unique multi-macrocycles, which exhibit behavior distinct from that of monocyclic structures (Fig. 1a).[5] For instance, Du *et al.* reported CPP-based bismacrocycles that exhibit dual-emission behavior, characterized by tunable aggregation-induced emission and enhanced chiroptical properties.[6] Similarly, Yam and Jiang have independently synthesized rigid and heterotopic bismacrocycles combining CPP and pillar[5]arene, showcasing remarkable luminescent and host–guest recognition properties (Fig. 1b).[7]
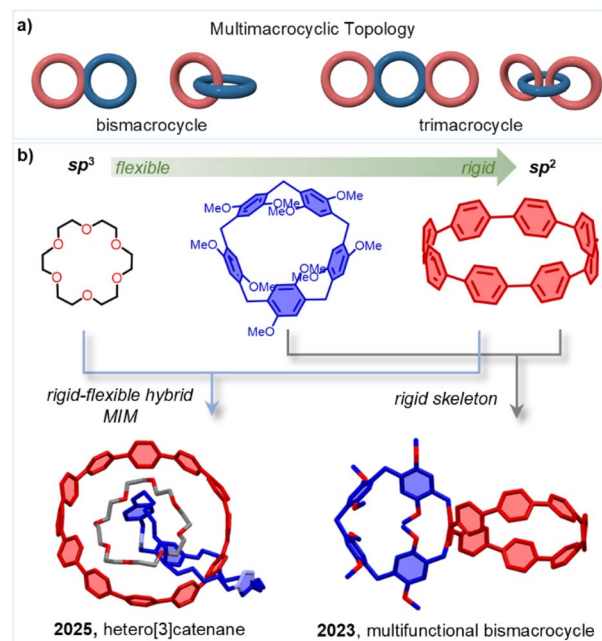
[a]College of Chemistry and Molecular Sciences, Henan University, Kaifeng 475004, P. R. China. E-mail: qiliu@henu.edu.cn; youzhixu@henu.edu.cn

[b]College of Public Health, Zhengzhou University, Zhengzhou 450001, P. R. China. E-mail: wudi22@zzu.edu.cn

[c]College of Chemistry, Zhengzhou University, Zhengzhou 450001, P. R. China

† Electronic supplementary information (ESI) available. CCDC 2393489 and 2393490. For ESI and crystallographic data in CIF or other electronic format see DOI: https://doi.org/10.1039/d5sc03476k

Fig. 1 (a) Illustration of two types of multimacrocyclic topology. (b) Selected examples of CPP-hybrid multimacrocycles.

Crown ethers are an intriguing class of macrocycles with flexible skeleton, renowned for their ability to selectively bind metal cations through coordination interactions and adeptly fabricate mechanically interlocked molecules (MIMs) *via* hydrogen bonding.[8] This synergy of properties offers exciting opportunities for innovative molecular designs. For example, we recently have reported the synthesis of a rare hetero[3]catenane using a ring-in-ring assembly strategy, incorporating unaltered [12]CPP, 24-crown-8 and a dibenzylammonium macrocycle (Fig. 1b).[9] To further explore the potential of the hydrids of CPPs and crown ethers. Herein, we present the synthesis of hybrid bis- and trimacrocycles combining CPPs and crown ethers. We then investigated their supramolecular properties and the application in organic electronic devices. Additionally, we conducted cell imaging and *in vitro* antitumor activity studies to evaluate their potential for biological applications.

Results and discussion

Synthesis and characterization

The pivotal intermediates for the synthesis of bis- and trimacrocycles are outlined in Fig. 2a. The hoop-shaped multimacrocycles **5**–**7**, varying in diameter, were successfully synthesized *via* Suzuki–Miyaura cross-coupling between
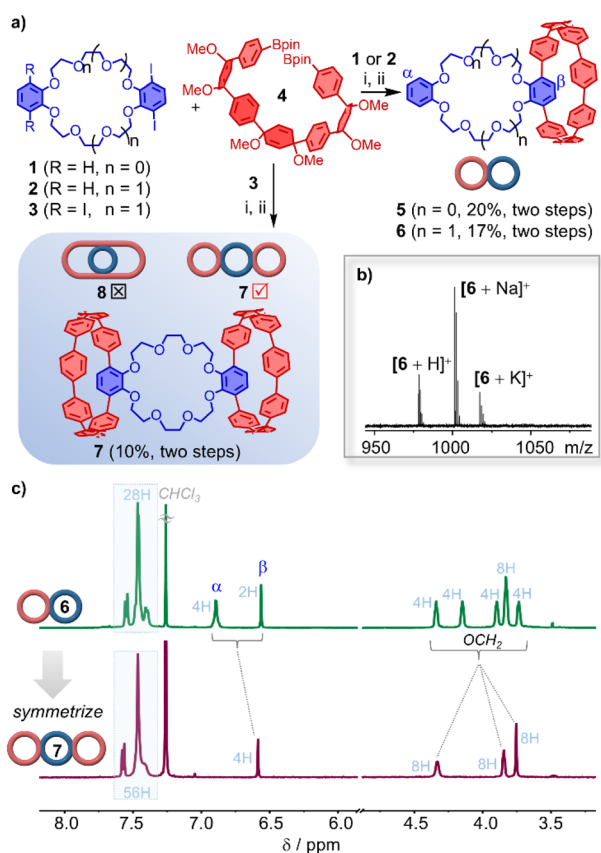

Fig. 2 Synthesis of crown ether-cycloparaphenylene hybrids. (a) Represent the key synthetic procedures. Reaction conditions: (i) [DPPF Pd G4], K_3PO_4, 1,4-dioxane–H_2O, 85 °C, 24 h. (ii) Sodium naphthalenide, THF, −78 °C, 2 h. (b) The HRMS-ESI of **6**. (c) Partial ^1H NMR spectra ($CDCl_3$, 298 K, 500 MHz) of **6** and **7**.

iodinated dibenzo-crown ethers **1**–**2** and diboronate **4**, followed by reductive aromatization. The [8]CPP-based bismacrocycles **5** and **6**, incorporating 18-crown-6 and 24-crown-8, were obtained in two steps with yields of 20% and 17%, respectively. Notably, the reaction between iodinated dibenzo-crown ethers **3** and diboronate **4** is theoretically expected to yield both the [8]CPP-based trimacrocycle **7** and the [16]CPP-based alternative topological multimacrocycle **8**. However, after separation and purification, combined with NMR and emission spectroscopy analysis, only the 24-crown-8-bridged trimacrocycle **7** was successfully synthesized, with a two-step yield of 10%. This outcome is presumably due to the mismatch between the torsional angle of substrate **4** and the size of **3**, which hinders the formation of the alternative multimacrocycle.[10]

These multimacrocycles were fully characterized by NMR spectroscopy and high-resolution mass spectrometry (HRMS) after standard workup and purification. The crown ether units within the macrocyclic backbone facilitated clear detection of sodium and potassium ion association in the mass spectra (Fig. 2b). Compared to bismacrocycle **6**, trimacrocycle **7** features two identical [8]CPP units flanking the dibenzo-24-crown-8 core, enhancing molecular symmetry, as confirmed by its ^1H NMR spectrum (Fig. 2c, and S1–S4†).

As shown in Fig. 3 (left), the structure of **6** can be recognized as an integration of the two classic macrocycles, dibenzo-24-crown-8 and [8]CPP. The two independent cavities do not overlap with each other, the distance between the two phenyl rings of dibenzo-24-crown-8 and the diameter of [8]CPP are calculated to be 10.5 Å and 10.4 Å, respectively. Then, we dissolved equimolar amounts of compounds **6** and KPF_6 in a 1 : 1 $CHCl_3$–MeOH solution and obtained single crystals of the metal complex **6**⊃K^+. Analyzing the X-ray crystal structure of complex **6**⊃K^+, we can see that the 24-crown-8 ring tightly encapsulates the potassium ion by folding, primarily *via* multiple electrostatic interactions, the average distance of O···K is 2.5 Å (Fig. 3, right). Due to the introduction of the 24-crown-8 ring, [8]CPP no longer presents ordered columnar packing,[11] but a random packing with no apparent supramolecular interactions between the complex molecules was found in the solid state (Fig. S5 and S6†). This also leads to **6** having better solubility in organic solvents.

Photophysical properties

The absorption spectra of multimacrocycles **5**, **6** and **7** closely resemble that of [8]CPP, exhibiting a primary absorption maximum around 335 nm and a shoulder near 400 nm, attributed to the HOMO → LUMO transition. The molar extinction coefficients (ε) at 335 nm for **5** ($7.8 \times 10^4 \, M^{-1} \, cm^{-1}$) and **6** ($8.5 \times 10^4 \, M^{-1} \, cm^{-1}$) are comparable to that of [8]CPP, whereas **7** ($1.3 \times 10^5 \, M^{-1} \, cm^{-1}$) exhibits approximately 1.5 times higher absorption. This increase suggests that the two CPP units in **7** behave as independent chromophores, consistent with Beer's Law, although possible excitonic coupling effects cannot be ruled out.

In dichloromethane at 298 K, **5**, **6** and **7** display fluorescence emission bands centered at 530 nm, 527 nm and 530 nm,
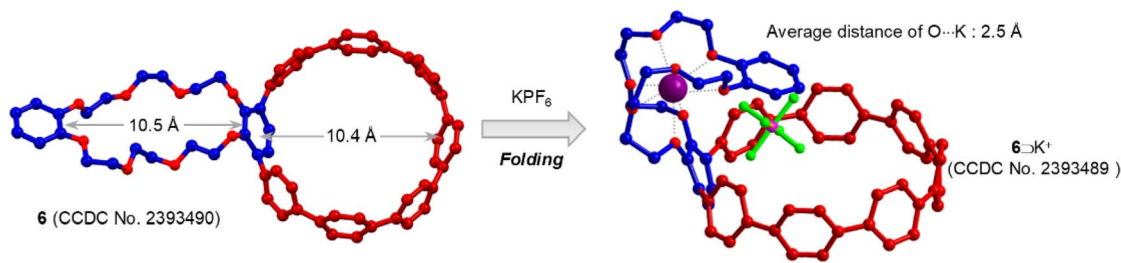
Fig. 3 X-ray crystal structure of **6** and the complex of **6**⊃K$^+$.

respectively, upon excitation at 340 nm (Fig. 4a and b). Compared to [8]CPP, these multimacrocycles exhibit a slight blue shift, which may arise from subtle structural distortions induced by the crown ether ring. Such distortions could slightly reduce effective π-conjugation, thereby increasing the energy gap between the excited and ground states.

More notably, their fluorescence quantum yields ($\Phi_F = 0.55$ for **5**, 0.58 for **6**, 0.60 for **7**) are significantly higher than that of [8]CPP ($\Phi_F = 0.10$),[3] indicating a strong enhancement in radiative emission efficiency. The fluorescence enhancement can be attributed to multiple factors. First, orbital symmetry breaking in the CPP backbone may increase the transition dipole moment, thereby enhancing radiative decay rates (Fig. 4c).[12] Second, the introduction of crown ether moieties may impose structural rigidity, reducing non-radiative relaxation pathways such as intramolecular rotations or vibrations. Time-resolved

fluorescence measurements reveal that the fluorescence lifetimes of **5** (4.2 ns), **6** (2.8 ns) and **7** (4.3 ns) are comparable to that of [8]CPP, suggesting that the increased fluorescence quantum yield is primarily due to suppression of non-radiative decay rather than an intrinsic increase in excited-state lifetime. In the solid state, **5**, **6** and **7** maintain Φ_F values of 16%, 14% and 18%, respectively, despite the potential for aggregation-caused quenching (ACQ). This suggests that the presence of crown ether substituents helps mitigate intermolecular π–π stacking, likely by introducing steric hindrance and restricting molecular aggregation.

Guest recognition and gas sensing

Analysis of the X-ray crystal structure of **6** revealed that the flexible crown ether backbone adopts a folded conformation. This structural feature led us to hypothesize that trimacrocycle **7** might serve as an effective host for fullerene recognition (Fig. S7 and Table S3†).[13] While [10]CPP is well known for encapsulating C_{60} *via* strong π–π interactions, the smaller size of [8]CPP generally results in weaker binding. Given the structural modifications introduced in **7**, we sought to evaluate its binding properties toward C_{60} through fluorescence quenching titrations in toluene.

The binding study revealed that **6**⊃C_{60} forms with an association constant ($K_A = (1.5 \pm 0.05) \times 10^5$ M^{-1}, Fig. S10†), which is significantly lower than [10]CPP⊃C_{60} (3.6×10^{-6} M^{-1})[14] but higher than unmodified [8]CPP, likely due to additional dispersion interactions introduced by the crown ether side chains. In contrast, titration experiments between **7** and C_{60} exhibited a 1:1 (host:guest) binding equilibrium, with the a much higher association constant ($K_{1:1} = (2.4 \pm 0.5) \times 10^6$ M^{-1}, Fig. 5a) compared to **6**⊃C_{60}. This suggests that **7** adopts a molecular tweezer-like conformation,[15] where its two CPP units cooperatively encapsulate the fullerene, significantly enhancing its binding affinity. DFT-optimized structures confirm that C_{60} sits symmetrically within the cavity of **7**, stabilized primarily by dispersion forces between the π-conjugated CPP units and the fullerene surface (Fig. S11 and Table S4†). Independent Gradient Model (IGM) analysis further highlights strong non-covalent interactions in the **7**⊃C_{60} complex, reinforcing the enhanced binding affinity observed experimentally (Fig. 5b).

The interactions and photophysical properties of CPP and C_{60} have been extensively studied. However, their potential applications in semiconductor devices remain underexplored.
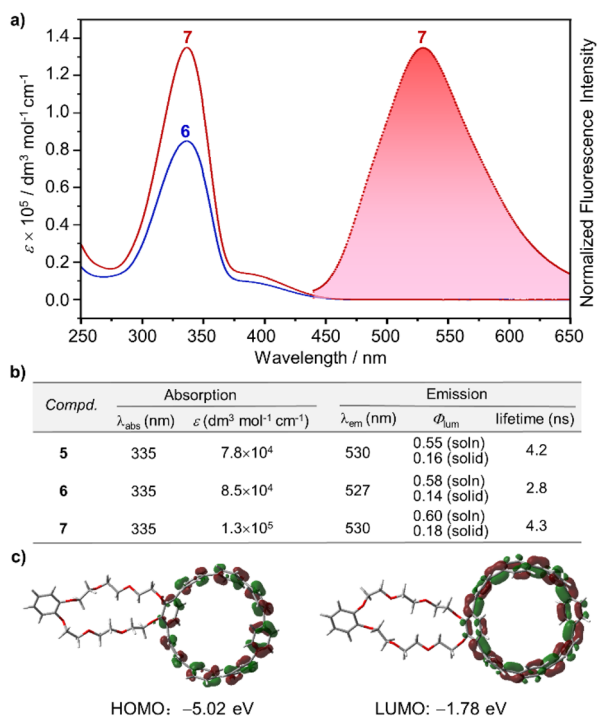

Fig. 4 (a) UV-vis absorbance (solid lines) and fluorescence (dashed lines) spectra for **6** and **7** (conc. 5.0×10^{-6} M in dichloromethane). (b) Selected photophysical properties of **5–7**. (c) Frontier molecular orbitals of **6** calculated at the B3LYP/6-31G(d) level of theory (isovalue 0.03).

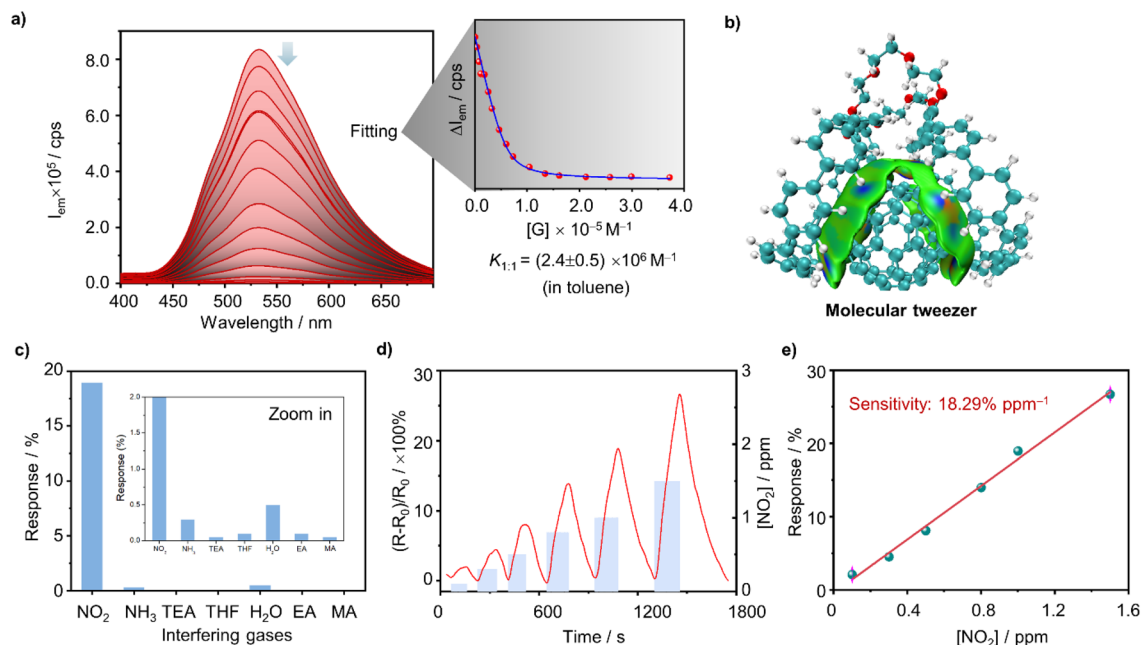| Compd.	Absorption		Emission		
	λ_{abs} (nm)	ε (dm^3 mol^{-1} cm^{-1})	λ_{em} (nm)	Φ_{lum}	lifetime (ns)
5	335	7.8×10^4	530	0.55 (soln) 0.16 (solid)	4.2
6	335	8.5×10^4	527	0.58 (soln) 0.14 (solid)	2.8
7	335	1.3×10^5	530	0.60 (soln) 0.18 (solid)	4.3

HOMO: −5.02 eV   LUMO: −1.78 eV

Fig. 5 (a) Fluorescence titrations between **7** (conc. 6.0×10^{-6} M^{-1}) and C$_{60}$ in toluene. Association constants were obtained by fitting the data according to a 1:1 (host : guest) stoichiometric model. (b) IGM analyses of the complexe of **7**⊃C$_{60}$ ($\delta g_{inter} = 0.003$). (c) Response of **7**⊃C$_{60}$ for different interfering gases (TEA: triethylamine; THF: tetrahydrofuran; EA: ethyl acetate; MA: methanol). (d) Dynamic response curves of **7**⊃C$_{60}$ toward 0.1–1.5 ppm NO$_2$. (e) Linear relationship of response *vs.* NO$_2$ concentration of **7**⊃C$_{60}$.

Therefore, we further investigated the use of CPP and its fullerene complexes in organic electronic devices. Thin film electrodes were fabricated on interdigital electrodes (IDEs) using the quasi-Langmuir–Shäfer (QLS) technique, which were then employed as chemiresistive gas sensors (CGS) for detecting hazardous gases (Fig. S12†).[16] The conductivity characteristics of **7** and the **7**⊃C$_{60}$ complex were initially assessed through *I–V* curves (Fig. S13†). Due to the incorporation of an electron transport mediator and the push–pull electronic effects between C$_{60}$ and **7**, the **7**⊃C$_{60}$ complex demonstrated significantly enhanced conductivity (6.37×10^{-7} S cm^{-1}) compared to **7** alone, making it more suitable for CGS applications.[17]

We applied the **7**⊃C$_{60}$-based chemiresistive sensor for detecting a variety of potential interfering gases. As shown in Fig. 5c, the **7**⊃C$_{60}$ complex exhibited a markedly higher response to NO$_2$ than to other test gases, highlighting its exceptional specificity toward NO$_2$. Subsequently, we examined the sensitivity of both **7**⊃C$_{60}$ and **7** to NO$_2$ in the concentration range of 0.1–1.5 ppm. As illustrated in Fig. 5d and S14,† the **7**⊃C$_{60}$ complex displayed superior response and recovery characteristics to NO$_2$ in this concentration range, attributable to its enhanced conductivity and the presence of the donor–acceptor (D–A) structure. Furthermore, as depicted in Fig. 5e, the **7**⊃C$_{60}$ complex exhibited a strong linear relationship with NO$_2$ concentrations from 0.1 to 1.5 ppm, with a sensitivity of 18.29% ppm^{-1}. Based on this, the limit of detection (LOD) for NO$_2$ was calculated to be 19 ppb, indicating the sensor's potential for practical applications. Additionally, the cyclic stability of the **7**⊃C$_{60}$ complex at 1 ppm NO$_2$ was evaluated, with results showing a coefficient of variation not exceeding

1.2%, demonstrating the excellent cyclic stability of the **7**⊃C$_{60}$-based sensor (Fig. S15†).

To further understand the significantly enhanced gas-sensing response of the **7**⊃C$_{60}$ complex compared to **7**, we first tested the transient photocurrent of both devices in air (Fig. 6a). The results revealed that the **7**⊃C$_{60}$ complex exhibited a higher current intensity under simulated sunlight compared to **7**, indicating that photo-generated charge carriers in the **7**⊃C$_{60}$ complex are more easily separated and directed for transport. This provides further evidence of a distinct D–A effect in the **7**⊃C$_{60}$ complex.[18] As shown in Fig. 6b, during the NO$_2$ detection process, **7** effectively captures and concentrates NO$_2$ molecules. Due to the D–A structure, the charge transfer barrier between the **7** and NO$_2$ is disrupted by C$_{60}$. As an electron transport mediator, C$_{60}$ facilitates efficient electron transfer to NO$_2$, leading to a significant decrease in the electron density on the **7**⊃C$_{60}$ complex. This, in turn, increases the resistance and enhances the gas-sensing response. Upon removal of NO$_2$ from

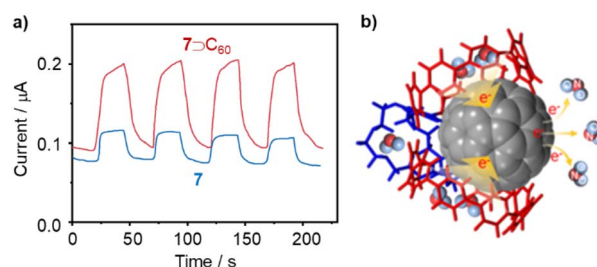**Fig. 6** (a) Photocurrent of the **7**⊃C$_{60}$ complex and **7** at 5 V. (b) The proposed sensing mechanism of **7**⊃C$_{60}$ for NO$_2$.
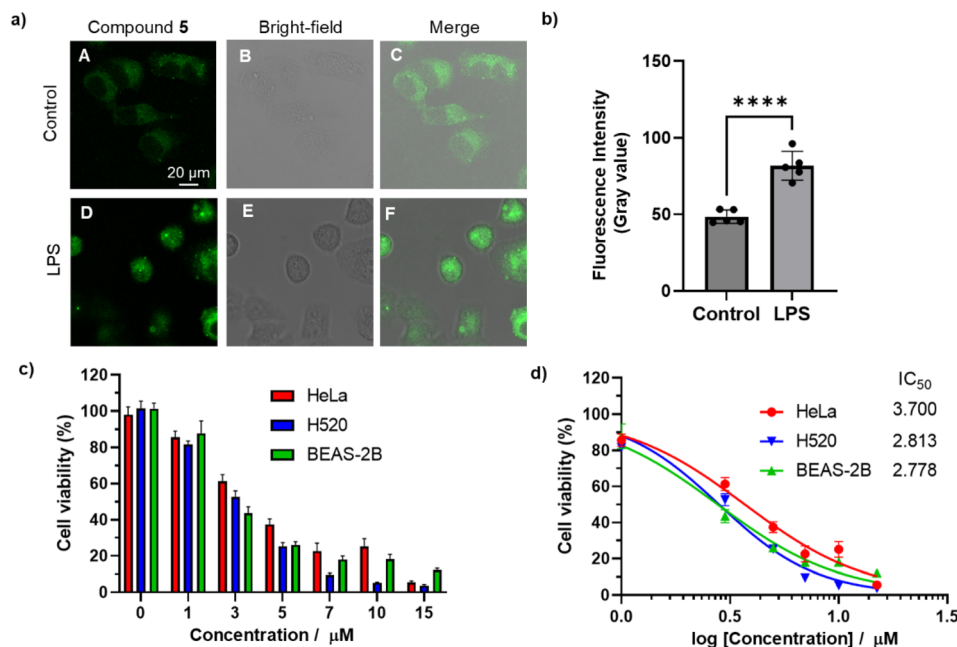
Fig. 7 (a) Confocal fluorescence imaging of HeLa cells. Control groups (A–C): the cells were incubated with 5 for 90 minutes. LPS groups (D and E): the cells were pretreated with LPS (1 µg mL^{-1}) for 30 minutes before incubating with 5. $\lambda_{ex} = 405$ nm, $\lambda_{em} = 500$–600 nm. (b) Comparison of the fluorescence intensity of the cells in (A) and (D). Data are expressed as the mean $\pm$ SD, $n = 5$. Statistical significance is denoted by **** ($p < 0.0001$). (c) Cell viability and (d) inhibition rates of HeLa, H520, and BEAS-2B cells with different concentrations of the compound (0, 1, 3, 5, 7, 10, and 15 µM). Data are expressed as mean $\pm$ SD, $n = 3$.

the $7 \supset C_{60}$ complex, the electrons released by NO_2 return to the complex, restoring the sensor's resistance to its baseline state. Moreover, the D–A structure ensures the directional transport of electrons, thereby enabling stable responses to NO_2 detection.

Biological application evaluation

Incorporating polar side-chain functionalization into the CPP ring may enhance the macrocycles' utility in biosensing and bioimaging applications.[19] Since compounds **5** and **6** exhibited similar properties, but **5** was synthesized more efficiently, and compound **7** showed poor solubility in polar solvents, bismacrocycle **5** was selected for cell imaging and *in vitro* antitumor activity studies to evaluate its biological potential. Fluorescence imaging with the HeLa cervical cancer cell line was conducted to assess the bismacrocycle's cellular uptake. After 90 minutes of incubation, weak green fluorescence was observed within the cells, indicating successful penetration of the cell membrane (Fig. 7a(A–C)). Lipopolysaccharide (LPS), a well-known inflammatory stimulus, induces reactive oxygen species (ROS) production in cells, increasing cytoplasmic viscosity and promoting inflammation.[20] When cells were pretreated with LPS (1 µg mL^{-1}) for 30 minutes before exposure to the bismacrocycle **5**, a marked increase in fluorescence intensity was observed (Fig. 7a(D and E)). This enhancement was significantly greater than that in the control group (Fig. 7b), suggesting the bismacrocycle's potential for identifying and distinguishing inflammatory cells. The observed increase in fluorescence after LPS pretreatment may be attributed to changes in cellular viscosity, which could facilitate the radiative transition of the compound in inflammatory cells.[21] This finding is important, as

it highlights the bismacrocycle's ability to detect and monitor inflammatory responses within cells.

Next, the cytotoxicity of the compound was evaluated in HeLa, H520 (lung cancer), and BEAS-2B (normal lung epithelial) cells using the MTT assay. As shown in Fig. 7c, the bismacrocycle **5** exhibited significant cytotoxicity across all cell lines at a minimal concentration of 3 µM after 24 hours of incubation. The half-maximal inhibitory concentration (IC_{50}) values for HeLa, H520, and BEAS-2B cells were determined to be 3.700, 2.813, and 2.778 µM, respectively (Fig. 7d). These relatively low IC_{50} values underscore the bismacrocycle's potent antitumor activity, which has not been previously reported in the literature.

The bismacrocycle's potent cytotoxicity at low concentrations, with IC_{50} values notably lower than those of comparable nanohoops, suggests a superior therapeutic index and emphasizes its potential as an effective anticancer agent. This is particularly significant given the growing demand for drugs with high potency. Collectively, these findings lay a strong foundation for advancing the compound as a novel imaging agent and anticancer therapeutic, with promising applications in the imaging and treatment of various cancer types. These results also demonstrate that compound **5** possesses remarkable bioactivity compared to other crown ether derivatives, which is attributed to the incorporation of cycloparaphenylene.[22]

Conclusion

In this study, we have successfully designed and synthesized a series of crown ether–CPP hybrid multimacrocycles and

explored their supramolecular properties, photophysical behavior, and biological applications. The integration of crown ethers into the CPP framework not only improves solubility and enhances fluorescence quantum yield but also introduces new binding sites that facilitate selective host–guest interactions. Notably, the trimacrocyclic hybrid adopts a molecular tweezer-like conformation, leading to a *ca.* 15-fold increase in fullerene binding affinity compared to its bismacrocyclic counterpart. This enhanced host–guest recognition behavior, supported by fluorescence quenching titrations and density functional theory (DFT) calculations, provides new insights into the design of high-affinity supramolecular receptors. Additionally, the fullerene complex was explored as a chemiresistive gas sensor for NO_2 detection. It showed improved conductivity and sensitivity with a LOD of 19 ppb, thanks to its D–A structure and fullerene's role as an electron transport mediator. The sensor also demonstrated excellent cyclic stability and reliable, directional electron transport for NO_2 detection.

The biological evaluation of these hybrid macrocycles further underscores their potential for biomedical applications. The bismacrocycle exhibits significant cytotoxicity against cancer cell lines at micromolar concentrations, with IC_{50} values lower than those of comparable nanohoops, highlighting its promise as a novel anticancer agent. Moreover, its fluorescence-based detection of inflammatory responses suggests potential applications in biosensing and imaging. These findings collectively demonstrate that crown ether–CPP hybrids represent a new class of multifunctional macrocycles with broad applicability in supramolecular sensing[23] and biochemistry.[24]

Data availability

The data supporting this article have been included as part of the ESI.†

Author contributions

Y. Xu proposed the concept. Y. Hu, T. Su and W. Shi carried out the synthesis of the compounds, conducted the characterizations, and analyzed the data. B. Li and M.-H. Li contributed to the analysis of single-crystal structures. Q. Liu and Y. Yu prepared the electronic devices and performed the sensing experiments. T. Li and D. Wu carried out cell imaging and *in vitro* antitumor activity studies. Y. Xu, Q. Liu and D. Wu wrote the manuscript. Y.-Q. Xu and S. Zhang contributed to the discussions and revisions of the manuscript.

Conflicts of interest

There are no conflicts to declare.

Acknowledgements

References

1 (a) T. Ogoshi, T. A. Yamagishi and Y. Nakamoto, *Chem. Rev.*, 2016, **116**, 7937–8002; (b) X. Chang, Y. Xu and M. von Delius, *Chem. Soc. Rev.*, 2024, **53**, 47–83; (c) Y.-J. Long, X.-N. Han, Y. Han and C.-F. Chen, *Chin. Chem. Lett.*, 2025, **36**, 110600; (d) Y. Yu, Y. Hu, C. Ning, W. Shi, A. Yang, Y. Zhao, Z.-Y. Cao, Y. Xu and P. Du, *Angew. Chem., Int. Ed.*, 2024, **63**, e202407034.

2 (a) T. D. Clayton, J. M. Fehr, T. W. Price, L. N. Zakharov and R. Jasti, *J. Am. Chem. Soc.*, 2024, **146**, 30607–30614; (b) Y. Xu, M. -Yi Leung, L. Yan, Z. Chen, P. Li, Y.-H. Cheng, M. H.-Y. Chan and V. W.-W. Yam, *J. Am. Chem. Soc.*, 2024, **146**, 13226–13235; (c) W. Shi, Y. Zhao and Y. Xu, *Trends Chem.*, 2025, **7**, 1–2.

3 E. R. Darzi and R. Jasti, *Chem. Soc. Rev.*, 2015, **44**, 6401–6410.

4 (a) Y. Li, H. Kono, T. Maekawa, Y. Segawa, A. Yagi and K. Itami, *Acc. Mater. Res.*, 2021, **2**, 681–691; (b) J. Malinčík, S. Gaikwad, J. P. Mora-Fuentes, M.-A. Boillat, A. Prescimone, D. Häussinger, A. G. Campaña and T. Šolomek, *Angew. Chem., Int. Ed.*, 2022, **61**, e202208591; (c) M. Hermann, D. Wassy and B. Esser, *Angew. Chem., Int. Ed.*, 2021, **60**, 15743–15766; (d) A. Stergiou, J. Rio, J. H. Griwatz, D. Arcon, H. A. Wegner, C. Ewels and N. Tagmatarchis, *Angew. Chem., Int. Ed.*, 2019, **58**, 17745–17750.

5 (a) X.-L. Chen, S.-Q. Yu, X.-H. Huang and H.-Y. Gong, *Molecules*, 2023, **28**, 6043; (b) Y. Zhang, D. Yang, S. H. Pun, H. Chen and Q. Miao, *Precis. Chem.*, 2023, **1**, 107–111; (c) J. He, M.-H. Yu, Z. Lian, Y.-Q. Fan, S.-Z. Guo, X.-N. Li, Y. Wang, W.-G. Wang, Z.-Y. Cheng and H. Jiang, *Chem. Sci.*, 2023, **14**, 4426–4433; (d) X. Zhang, Y. Xu and P. Du, *Acc. Mater. Res.*, 2025, **6**, 399–410; (e) G. Li, L.-L. Mao, J.-N. Gao, X. Shi, Z.-Y. Huo, J. Yang, W. Zhou, H. Li, H.-B. Yang, C.-H. Tung, L.-Z. Wu and H. Cong, *Angew. Chem., Int. Ed.*, 2025, **64**, e202419435; (f) Y. Yang, O. Blacque, S. Sato and M. Juríček, *Angew. Chem., Int. Ed.*, 2021, **60**, 13529–13535; (g) L. Ren, Y. Han, X. Hou, Y. Zou, T. Jiao and J. Wu, *CCS Chem.*, 2024, **6**, 2758–2769; (h) X.-W. Chen, Q.-S. Deng, B.-H. Zheng, J.-F. Xing, H.-R. Pan, X.-J. Zhao and Y.-Z. Tan, *J. Am. Chem. Soc.*, 2024, **146**, 31665–31670; (i) K. Li, S. Yoshida, R. Yakushiji, X. Liu, C. Ge, Z. Xu, Y. Ni, X. Ma, J. Wu, S. Sato and Z. Sun, *Chem. Sci.*, 2024, **15**, 18832–18839; (j) Y. Liu, P. Lei, Y. Feng, S. Fu, X. Liu, S. Zhang, B. Tu, C. Chen, Y. Li, L. Wang and Q.-D. Zeng, *Chin. Chem. Lett.*, 2024, **35**, 109571; (k) K. Senthilkumar, M. Kondratowicz, T. Lis, P. J. Chmielewski, J. Cybinska, J. L. Zafra, J. Casado, T. Vives, J. Crassous, L. Favereau and M. Stępień, *J. Am. Chem. Soc.*, 2019, **141**, 7421–7427.

6 X. Zhang, H. Liu, G. Zhuang, S. Yang and P. Du, *Nat. Commun.*, 2022, **13**, 3543.

7 (a) Y. Xu, F. Steudel, M. Leung, B. Xia, M. von Delius and V. W-W Yam, *Angew. Chem., Int. Ed.*, 2023, **62**, e202302978;

(b) Y. Fan, S. Fan, L. Liu, S. Guo, J. He, X. Li, Z. Lian, W. Guo, X. Chen, Y. Wang and H. Jiang, *Chem. Sci.*, 2023, **14**, 11121–11130; (c) Y. Zhou, G. Zhuang and P. Du, *Chin. Chem. Lett.*, 2024, **35**, 108593.

8 (a) J. E. M. Lewis, P. D. Beer, S. J. Loeb and S. M. Goldup, *Chem. Soc. Rev.*, 2017, **46**, 2577–2591; (b) L. Chen, X. Sheng, G. Li and F. Huang, *Chem. Soc. Rev.*, 2022, **51**, 7046–7065; (c) N. H. Evans and P. D. Beer, *Chem. Soc. Rev.*, 2014, **43**, 4658–4683; (d) A. Goswami, S. Saha, P. K. Biswas and M. Schmittel, *Chem. Rev.*, 2019, **120**, 125–199.

9 W. Shi, Y. Hu, L. Leanza, Y. Shchukin, P. A. Hoffmann, M. Li, C. Ning, Z.-Y. Cao, Y.-Q. Xu, P. Du, M. von Delius, G. M. Pavan and Y. Xu, *Angew. Chem., Int. Ed.*, 2025, **64**, e202421459.

10 H. Zhong, K. Lan, J. Ming, D. Zhang and C. Cheng, *Org. Lett.*, 2025, **27**, 4349–4354.

11 J. Xia, J. W. Bacon and R. Jasti, *Chem. Sci.*, 2012, **3**, 3018–3021.

12 T. C. Lovell, C. E. Colwell, L. N. Zakharov and R. Jasti, *Chem. Sci.*, 2019, **10**, 3786–3790.

13 (a) Y. Xu and M. von Delius, *Angew. Chem., Int. Ed.*, 2020, **59**, 559–573; (b) C. García-Simón, M. Costas and X. Ribas, *Chem. Soc. Rev.*, 2016, **45**, 40–62.

14 T. Iwamoto, Y. Watanabe, T. Sadahiro, T. Haino and S. Yamago, *Angew. Chem., Int. Ed.*, 2011, **50**, 8342–8344.

15 (a) A. Sacristan-Martin, H. Barbero, S. Ferrero, D. Miguel, R. Garcia-Rodriguez and C. M. Alvarez, *Chem. Commun.*, 2021, **57**, 11013–11016; (b) B. Scholz, A. S. Oshchepkov, O. Papaianina, C. Ruppenstein, V. A. Akhmetov, D. I. Sharapa, K. Y. Amsharov and M. E. Pérez-Ojeda, *Chem.–Eur. J.*, 2023, **29**, e202302778; (c) M. S. Mirzaei, S. Mirzaei, V. M. E. Castro, C. Lawrence and R. H. Sánchez, *Chem. Commun.*, 2024, **60**, 14236–14239.

16 Y. Zhang, Q. Liu, Q. Sun, H. Li, J. Shen, H. Liu, W. Chen, Y. Zhang and Y. Chen, *ACS Sens.*, 2023, **8**, 4353–4363.

17 Q. Liu, Q. Li, Y. Li, T. Su, B. Hou, Y. Zhao and Y. Xu, *Angew. Chem., Int. Ed.*, 2025, **64**, e202502536.

18 (a) Q. Liu, Q. Sun, H. Li, Y. Zhang, L. Feng, W. Chen and Y. Chen, *Sens. Actuators, B*, 2025, **428**, 137250; (b) K. Ding, K. Zhang, X. Liu, Q. Xu, X. Cheng, M. Yao, W. Wang, Y. Zeng, T. Ye, Y. He, W. Lin, R. Zhou, Ya. Chen and S. Li, *ACS Nano*, 2025, **19**, 8238–8254.

19 (a) K. Günther, H. Kono, H. Shudo, D. Shimizu, R. Isoda, M. Nakamura, A. Yagi, K. Amaike and K. Itami, *Angew. Chem., Int. Ed.*, 2025, **64**, e202414645; (b) B. M. White, Y. Zhao, T. E. Kawashima, B. P. Branchaud, M. D. Pluth and R. Jasti, *ACS Cent. Sci.*, 2018, **4**, 1173–1178.

20 (a) Y. Zhang, Z. Li, W. Hu and Z. Liu, *Anal. Chem.*, 2019, **91**, 10302–10309; (b) Y.-Y. Li, J.-L. Hu, J.-R. Wu, Y.-R. Wang, A.-H. Zhang, Y.-W. Tan, Y.-J. Shang, T. Liang, M. Li, Y.-L. Meng and Y.-F. Kang, *Biosens. Bioelectron.*, 2024, **254**, 116233.

21 (a) S. Feng, S. Gong, Z. Zheng and G. Feng, *Sens. Actuators, B*, 2022, **351**, 130940; (b) W.-N. Wu, Y.-F. Song, X.-L. Zhao, Y. Wang, Y.-C. Fan, Z.-H. Xu and T. D. James, *Chem. Eng. J.*, 2023, **464**, 142553.

22 H. Zhang, R. Ye, Y. Mu, T. Li and H. Zeng, *Nano Lett.*, 2021, **21**, 1384–1391.

23 (a) Q. Chen and K. Zhu, *Chem. Soc. Rev.*, 2024, **53**, 5677–5703; (b) Z. Zhang, J. Zhao and X. Yan, *Acc. Chem. Res.*, 2024, **57**, 992–1006; (c) C. Wang, L. Xu, Z. Jia and T.-P. Loh, *Chin. Chem. Lett.*, 2024, **35**, 109075; (d) M. Regehly, Y. Garmshausen, M. Reuter, N. F. König, E. Israel, D. P. Kelly, C.-Y. Chou, K. Koch, B. Asfari and S. Hecht, *Nature*, 2020, **588**, 620–624; (e) Z.-B. Tang, L. Bian, X. Miao, H. Gao, L. Liu, Q. Jiang, D. Shen, L. Xu, A. C.-H. Sue, X. Zheng and Z. Liu, *Nat. Synth.*, 2025, DOI: **10.1038/s44160-025-00791-x**.

24 K. Chinner, N. Grabicki, R. Hamaguchi, M. Ikeguchi, K. Kinbara, S. Toyoda, K. Sato and O. Dumele, *Chem. Sci.*, 2024, **15**, 16367–16376.